INTERNATIONAL JOURNAL FOR NUMERICAL METHODS IN FLUIDS, VOL. 23, 1133–1144 (1996)

CALCULATION OF WALL-BOUNDED COMPLEX FLOWS AND FREE SHEAR FLOWS

T.-H. SHIH AND J. ZHU

Center for Modelling of Turbulence and Transition, ICOMP, OAI, NASA Lewis Research Center, Cleveland, OH, U.S.A.

AND

JOHN L. LUMLEY

Cornell University, Ithaca, NY, U.S.A.

SUMMARY

Various wall-bounded flows with complex geometries and free shear flows have been studied with a newly developed realizable Reynolds stress algebraic equation model. The model development is based on the invariant theory in continuum mechanics. This theory enables us to formulate a general constitutive relation for the Reynolds stresses. Pope (*J. Fluid Mech.*, **72**, 331–340 (1975)) was the first to introduce this kind of constitutive relation to turbulence modelling. In our study, realizability is imposed on the truncated constitutive relation to determine the coefficients so that, unlike the standard k–ε eddy viscosity model, the present model will not produce negative normal stresses in any situations of rapid distortion. The calculations based on the present model have shown encouraging success in modelling complex turbulent flows.

KEY WORDS: turbulence models; realizability; complex flows

1. INTRODUCTION

The present study concentrates on complex turbulent shear flows which are of great interest in propulsion systems. These flows are backward-facing step flows, confined coflowing jets, confined swirling coaxial jets, U-duct flows and diffuser flows. Most of these flows have complex structures. For example, the confined coflowing jet combines several types of flow structures, such as the shear layer, jet, recirculation, separation and reattachment. Accurate prediction of these flows is of great importance for engine design in all its key elements. Turbulent free shear flows (such as mixing layers, planar and round jets) have also been studied for the purpose of examining the performance of turbulence models in different benchmark flows.

The turbulence model used in this study is a newly developed realizable Reynolds stress algebraic equation model which is fundamentally different from the traditional algebraic Reynolds stress models. The present model is developed using the invariance theory in continuum mechanics. This theory leads to a general constitutive relation for the Reynolds stress tensor $\overline{u_i u_j}$ in terms of the mean deformation rate tensor $U_{i,j}$ and the turbulent velocity and length scales characterized by the turbulent kinetic energy k and its dissipation rate ε. Pope[1] applied this kind of constitutive relation to Rodi's algebraic Reynolds stress formulation in conjunction with the LRR second-order closure model[2] and obtained an explicit algebraic expression for the Reynolds stresses for a two-dimensional mean flow field. Taulbee[3] was able to extend this method to a general three-dimensional flow. We notice that in

CCC 0271–2091/96/111133–12

Received February 1995
Revised February 1996

Rodi's algebraic Reynolds stress formulation, some assumed concepts are in general not valid for most turbulent shear flows, e.g. the assumption of constant anisotropy of the Reynolds stresses and neglect of turbulent transport of second moments. These assumptions may bring large errors to turbulence modelling. In addition, an inappropriate second-order closure model would also add errors to this type of model. In this study, Rodi's formulation was not used. We directly impose realizability on the constitutive relation for the Reynolds stresses to determine the coefficients in the relation. As a result, a realizable explicit expression for the Reynolds stresses is obtained for general three-dimensional turbulent flows. Some model constants are fine-tuned against a backward-facing step flow and then tested in other flows.

The calculations are performed with a conservative finite volume method.[4] Grid-independent and low-numerical-diffusion solutions are obtained by using differencing schemes of second-order accuracy on sufficiently fine grids. For wall-bounded flows the standard wall function approach[5] is used for wall boundary conditions. The results are compared in detail with experimental data for both mean and turbulent quantities. Calculations using the standard k–ε eddy viscosity model are also carried out for the purpose of comparison. The comparison shows that the present realizable Reynolds stress algebraic equation model significantly improves the predictive capability of k–ε-equation-based models, especially for flows involving massive separations of strong shear layers. In these situations the standard eddy viscosity model overpredicts the eddy viscosity and hence fails to accurately predict the wall shear stress, separation, recirculation, etc. We find that the success of the present model in modelling the above-mentioned complex flows is largely due to its effective eddy viscosity formulation which accounts for the effect of mean shear rates. According to the present model, the effective eddy viscosity will be significantly reduced by the mean strain rate and maintained at a correct level to mimic the complex flow structures.

2. TURBULENCE MODEL

2.1. Constitutive relation

Constitutive relations for the Reynolds stresses were derived by several researchers.[1,6,7] Shih and Lumley[8] used the invariant theory in continuum mechanics and the generalized Cayley–Hamilton formulation[9] to derive a more (perhaps the most) general constitutive relation for the Reynolds stresses under the assumption that the Reynolds stresses are dependent only on the mean velocity gradients and the characteristic scales of turbulence characterized by the turbulent kinetic energy k and its dissipation rate ε. This relation is

$$\begin{aligned}\overline{u_i u_j} = {} & \tfrac{2}{3} k\delta_{ij} + 2a_2 \frac{K^2}{\varepsilon}(U_{i,j} + U_{j,i} - \tfrac{2}{3} U_{i,i}\delta_{ij}) \\ & + 2a_4 \frac{K^3}{\varepsilon^2}(U^2_{i,j} + U^2_{j,i} - \tfrac{2}{3}\Pi_1\delta_{ij}) \\ & + 2a_6 \frac{K^3}{\varepsilon^2}(U_{i,k}U_{j,k} - \tfrac{1}{3}\Pi_2\delta_{ij}) \\ & + 2a_7 \frac{K^3}{\varepsilon^2}(U_{k,i}U_{k,j} - \tfrac{1}{3}\Pi_2\delta_{ij}) \\ & + 2a_8 \frac{K^4}{\varepsilon^3}(U_{i,k}U^2_{j,k} + U^2_{i,k}U_{j,k} - \tfrac{2}{3}\Pi_3\delta_{ij}) \\ & + 2a_{10} \frac{K^4}{\varepsilon^3}(U_{k,i}U^2_{k,j} + U_{k,j}U^2_{k,i} - \tfrac{2}{3}\Pi_3\delta_{ij})\end{aligned}$$

$$
\begin{aligned}
&+2a_{12}\frac{K^5}{\varepsilon^4}(U^2_{i,k}U^2_{j,k}-\tfrac{1}{3}\Pi_4\delta_{ij})\\
&+2a_{13}\frac{K^5}{\varepsilon^4}(U^2_{k,i}U^2_{k,j}-\tfrac{1}{3}\Pi_4\delta_{ij})\\
&+2a_{14}\frac{K^5}{\varepsilon^4}(U_{i,k}U_{l,k}U^2_{l,j}+U_{j,k}U_{l,k}U^2_{l,i}-\tfrac{2}{3}\Pi_5\delta_{ij})\\
&+2a_{16}\frac{K^6}{\varepsilon^5}(U_{i,k}U^2_{l,k}U^2_{l,j}+U_{j,k}U^2_{l,k}U^2_{l,i}-\tfrac{2}{3}\Pi_6\delta_{ij})\\
&+2a_{18}\frac{K^7}{\varepsilon^6}(U_{i,k}U_{l,k}U^2_{l,m}U^2_{j,m}+U_{j,k}U_{l,k}U^2_{l,m}U^2_{i,m}-\tfrac{2}{3}\Pi_7\delta_{ij}),
\end{aligned}
\tag{1}
$$

where

$$
\begin{aligned}
&\Pi_1=U_{i,k}U_{k,i}, \quad \Pi_2=U_{i,k}U_{i,k}, \quad \Pi_3=U_{i,k}U^2_{i,k}, \quad \Pi_4=U^2_{i,k}U^2_{i,k},\\
&\Pi_5=U_{i,k}U_{l,k}U^2_{l,i}, \quad \Pi_6=U_{i,k}U^2_{l,k}U^2_{l,i}, \quad \Pi_7=U_{i,k}U_{l,k}U^2_{l,m}U^2_{i,m}.
\end{aligned}
\tag{2}
$$

Equation (1) contains 11 undetermined coefficients which are generally scalar functions of various invariants of the tensors in question, e.g. $S_{ij}S_{ij}$ (strain rate) and $\Omega_{ij}\Omega_{ij}$ (rotation rate) which are $(\Pi_2+\Pi_1)/2$ and $(\Pi_2-\Pi_1)/2$ respectively. The detailed forms of these scalar functions must be determined by other model constraints such as realizability and by experimental data.

It is noticed that the standard k–ε eddy viscosity model corresponds to the first two terms on the right-hand side of (1). Both the two-scale direct interaction approximation approach[6] and the RNG method[7] also provided a relation which is the first five terms on the right-hand side of (1).

In this study, for simplicity we truncate equation (1) to its quadratic tensorial form, which is of the same form as those developed by Yoshizawa[6] and Rubinstein and Barton.[7]

2.2. *Realizability*

Realizability,[10,11] defined as the requirement of the non- negativity of turbulent normal stresses and the Schwarz inequality between any fluctuating quantities, is a basic physical and mathematical principle that the solution of any turbulence model equation should obey. It also represents a minimal requirement to prevent a turbulence model from producing unphysical results. In the following, this principle will be applied to the truncated constitutive relation (1) to derive constraints on its coefficients.

Let us first consider a two-dimensional pure mean deformation in which the deformation rate tensor contains only non-zero diagonal components, i.e.

$$U_{i,j}=0 \quad \text{if} \quad i\neq j.$$

In this case the normal stress $\overline{u_1u_1}$ can be written as

$$\frac{\overline{u_1u_1}}{2k}=\tfrac{1}{3}+2a_2\frac{k}{\varepsilon}U_{1,1}+\tfrac{1}{3}(2a_4+a_6+a_7)\frac{k^2}{\varepsilon_2}(U_{1,1})^2.$$

If we define a time scale ratio of the turbulent to the mean strain rate as $\eta=Sk/\varepsilon$, where $S=\sqrt{(2S_{ij}S_{ij})}$, the above equation can be written as

$$\frac{\overline{u_1u_1}}{2k}=\tfrac{1}{3}+a_2\eta+\tfrac{1}{12}(2a_4+a_6+a_7)\eta^2.$$

Physically, we know that $\overline{u_1u_1}$ will decrease owing to the stretching by $U_{1,1}$. However, by realizability, $\overline{u_1u_1}$ should not be driven to negative values. Therefore we require that

$$\frac{\overline{u_1u_1}}{2k}\to 0 \quad \text{if} \quad \eta\to\infty, \qquad \left(\frac{\overline{u_1u_1}}{2k}\right)_{,\eta}\to 0 \quad \text{if} \quad \eta\to\infty.$$

These physically necessary conditions are called the realizability conditions. Similar analysis of $\overline{u_2u_2}$ and $\overline{u_3u_3}$ also leads to the above conditions. In addition, it should be mentioned that the above analysis also holds for the situation of a three- dimensional pure strain rate. These conditions can be satisfied in several ways, of which the simplest is perhaps the following:

$$2a_2 = -\frac{\frac{2}{3}}{A_1+\eta}, \qquad 2a_4 = \frac{C_{\tau 1}}{A_2+\eta^3+\xi^3}, \qquad 2a_6 = \frac{C_{\tau 2}}{A_2+\eta^3+\xi^3}, \qquad 2a_7 = \frac{C_{\tau 3}}{A_2+\eta^3+\xi^3},$$

where $\xi = \Omega k/\varepsilon$, $\Omega = (2\Omega^*_{ij}\Omega^*_{ij})^{1/2}$, $\Omega^*_{ij} = (U_{i,j}-U_{j,i})/2 + 4\varepsilon_{mji}\omega_m$ and ω_m represents the rotation of the co-ordinate frame. A_1, A_2, $C_{\tau 1}$, $C_{\tau 2}$ and $C_{\tau 3}$ will be taken as constants and determined by comparison calculations with experiments.

It can be seen from the above analysis that realizability cannot be fully satisfied if the model coefficients a_2–a_7 are taken as constant, such as those in the standard k–ε model and some anisotropic models, e.g. the model of Speziale.[12] In fact, these models satisfy realizability only in the weak sese, i.e. they only ensure the positivity of the sum of the normal Reynolds stresses. For more detailed discussion about model coefficients see Reference 13.

2.3. *Model equations*

The realizable Reynolds stress algebraic equation model can be written as

$$\begin{aligned}\overline{u_iu_j} = {} & \tfrac{2}{3}k\delta_{ij} - \nu_t(U_{i,j}+U_{j,i}) \\ & + \frac{C_{\tau 1}}{A_2+\eta^3+\xi^3}\frac{k^3}{\varepsilon^2}(U_{i,k}U_{k,j}+U_{j,k}U_{k,i}-\tfrac{2}{3}\Pi_1\delta_{ij}) \\ & + \frac{C_{\tau 2}}{A_2+\eta^3+\xi^3}\frac{k^3}{\varepsilon^2}(U_{i,k}U_{j,k}-\tfrac{1}{3}\Pi_2\delta_{ij}) \\ & + \frac{C_{\tau 3}}{A_2+\eta^3+\xi^3}\frac{k^3}{\varepsilon^2}(U_{k,i}U_{k,j}-\tfrac{1}{3}\Pi_2\delta_{ij}). \end{aligned} \tag{3}$$

Two quantities, the turbulent kinetic energy k and its dissipation rate ε, remain to be determined in (3). To this end we use the standard k–ε model equations

$$k_{,t} + U_jk_{,j} = \left[\left(\nu + \frac{\nu_t}{\sigma_k}\right)k_{,j}\right]_{,j} - \overline{u_iu_j}U_{i,j} - \varepsilon,$$

$$\varepsilon_{,t} + U_j\varepsilon_{,j} = \left[\left(\nu + \frac{\nu_t}{\sigma_\varepsilon}\right)\varepsilon_{,j}\right]_{,j} - C_{\varepsilon 1}\frac{\varepsilon}{k}\overline{u_iu_j}U_{i,j} - C_{\varepsilon 2}\frac{\varepsilon^2}{k},$$

where

$$\nu_t = C_\mu\frac{k^2}{\varepsilon}, \qquad C_\mu = \frac{\frac{2}{3}}{A_1+\eta}.$$

The coefficients $C_{\varepsilon 1}$, $C_{\varepsilon 2}$, σ_k and σ_ε assume their standard values

$$C_{\varepsilon 1} = 1{\cdot}44, \qquad C_{\varepsilon 2} = 1{\cdot}92, \qquad \sigma_k = 1, \qquad \sigma_\varepsilon = 1{\cdot}3$$

and the other coefficients are taken as

$$C_{\tau1} = -4, \quad C_{\tau2} = 13, \quad C_{\tau3} = -2, \quad A_1 = 5{\cdot}5, \quad A_2 = 1000.$$

These values are calibrated against the backward-facing step flow of Driver and Seegmiller,[14] for which a complete set of experimental data is available for both mean and turbulent quantities, and they are also found to be appropriate for other complex flows studied in this work.

3. APPLICATIONS

3.1. *Diffuser flows*

Two conical diffuser flows were calculated, one with an 8° total angle[15] and the other 10°.[16] In both cases the flows undergo strong adverse pressure gradients but remain attached. Although the flow configuration looks simple, it is not easy to calculate this type of flow accurately, especially for the boundary layer quantities. Figure 1 shows the variation in calculated and measured wall friction coefficients C_f with the axial distance x/R_0 (R_0 is the inlet duct radius). It is seen that the result of the present model is in good agreement with the experimental data, while the standard k–ε (SKE) model overpredicts C_f along almost the entire length of the diffuser. The calculated and measured displacement thicknesses δ^* are compared in Figure 2. The comparison shows that the SKE model gives a good prediction in the upstream region but deviates significantly from the experiment downstream; the present model prediction is good in the whole region. Figure 3 shows the

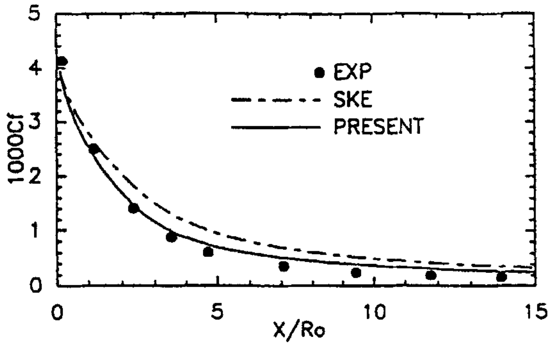

Figure 1. Wall friction coefficient (case of Trupp *et al.*[15])

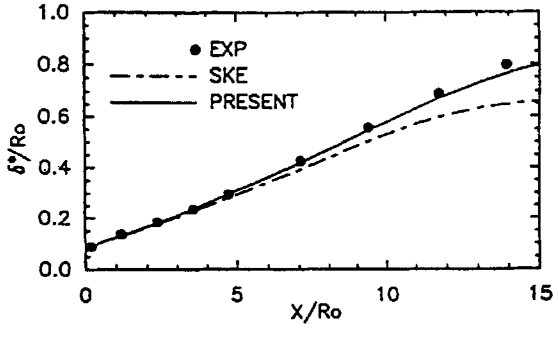

Figure 2. Displacement thickness (case of Trupp *et al.*[15])

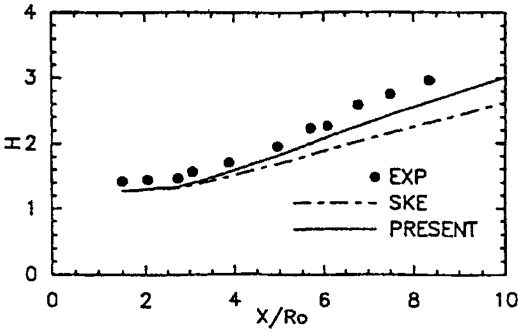

Figure 3. Shape factor (case of Fraser[16])

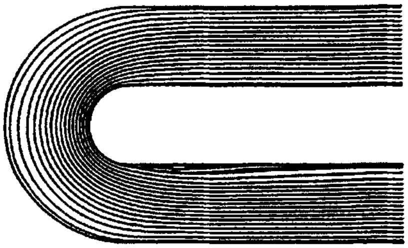

Figure 4. Streamlines

Table I. Comparison of reattachment points

Case	Measurement	SKE	Present
DS	6·26	4·99	5·82
KKJ	$7 \pm 0{\cdot}5$	6·35	7·35

comparison of calculated and measured shape factors H. This is the case in which the worst agreement with the measurement has been found for both models. Nevertheless, the present model still performs considerably better than does the SKE model.

3.2. *U-duct flow*

This case is the experiment of Monson *et al.*[17] conducted in a 180° planar turnaround duct. It features flow with large streamline curvature. Calculations are compared with the experiment at a flow Reynolds number of 10^6. Figure 4 shows the streamlines computed with the present model. A small separation region is found at the bend exit. However, the SKE model does not predict the flow separation. Figure 5 shows the comparison of calculated and measured C_f along the inner wall. The bend is located in the region $21{\cdot}7 \leqslant s/H \leqslant 24{\cdot}8$. Both models are seen to behave in the same manner and produce large discrepancies in the bend region. The reason for this may be partially due to the use of the wall function, which does not respond to the severe pressure gradient.

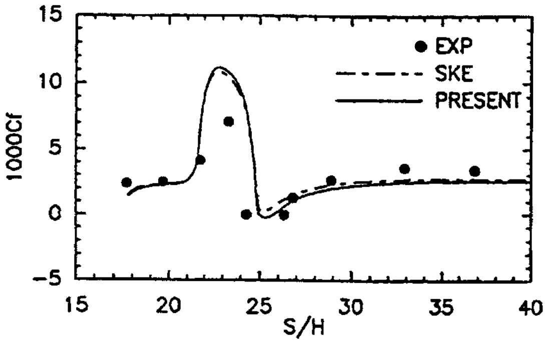

Figure 5. Friction coefficient along inner wall

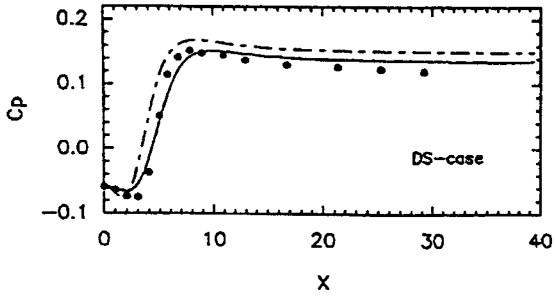

Figure 6. Pressure coefficient along bottom wall (legend as in Figure 5)

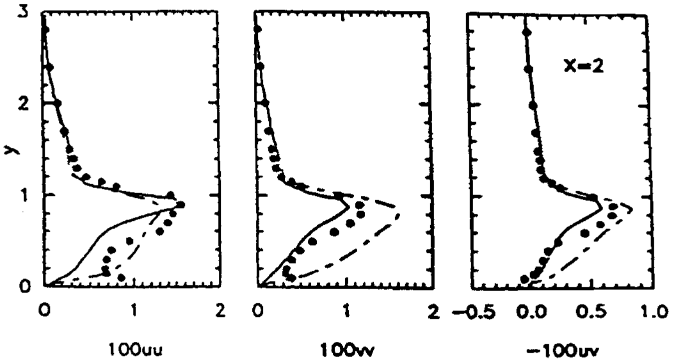

Figure 7. Turbulent stress profiles (legend as in Figure 5)

3.3. *Backward-facing step flows*

Two backward-facing step flows, measured by Driver and Seegmiller[14] and Kim *et al.*,[18] were calculated. The former (DS case) has a smaller and the latter (KKJ case) a larger step expansion. The computed and measured reattachment points are compared in Table I. The calculated reattachment point from the present model agrees well with the experiments. Figure 6 shows the comparison of computed and measured static pressure coefficients C_p along the bottom wall. The SKE model is seen to predict a premature pressure rise, which is consistent with its underprediction of the reattachment length, while the present model captures the pressure rise quite well. Figure 7 shows the comparisons of predicted and measured turbulent stresses $\overline{uu}$, $\overline{vv}$ and $\overline{uv}$ at the location $x = 2$, which is in the recirculation region. In the KKJ case no reliable experimental data exist for the turbulent stresses due to the unsteadiness of the flow. The experimental data of the DS case are considered more reliable because of the smaller unsteadiness of the flow. As compared with the results of the SKE model in Figure 7, it is seen that the anisotropic terms in the present model increase $\overline{uu}$ and decrease $\overline{vv}$, leading to significant improvements in both $\overline{uu}$ and $\overline{vv}$ except in the near-wall region. On the other hand, the anisotropic terms have little impact on $\overline{uv}$. The improvement obtained by the present model for $\overline{uv}$ is mainly due to the reduction in C_μ by strain rate.

3.4. *Confined jets*

The general features of confined jets, the experiments of Barchilon and Curtet,[19] are sketched in Figure 8. At the entrance, two uniform flows, a jet of larger velocity and an ambient stream of smaller velocity, are discharged into a cylindrical duct of diameter D_0. The inlet flow conditions can be characterized by the Craya–Curtet number C_t. The experiment shows that recirculation occurs when $C_t < 0{\cdot}96$. For a given geometry, recirculation as well as adverse pressure gradients can be intensified by reducing the value of C_t at the entrance. The separation and reattachment points of the predicted recirculation bubbles are compared with the experimental data in Figure 9. The experiment indicated that as C_t decreases, the separation point moves upstream while the reattachment point remains practically unchanged. The present model captures this feature well and predicts both the separation and reattachment points much better than does the SKE model. The variation in the pressure coefficient C_p along the duct wall is shown in Figure 10. The pressure distribution is governed by the jet entrainment as well as the contraction and expansion of the flow caused by the recirculation bubble. The decrease in the ambient velocity induced by the entrainment gives rise to an adverse pressure gradient, while the contraction of streamlines produces the opposite effect. These two mechanisms interact more intensely with each other as C_t decreases and cause the pressure to vary little in the region upstream of the centre of the recirculation bubble. However, in the downstream part of the recirculation bubble the deceleration of the flow sets up an adverse pressure gradient, the slope of which becomes steeper as C_t decreases. Therefore the ability to capture the location of the recirculation centre will have a direct impact on the prediction of the pressure. Regarding the comparison between predictions and experiments, it is seen that although both models predict practically the same total pressure rises which are in excellent agreement with the measurements, the present model captures the steep pressure gradients better than does the SKE model for all the C_t-values.

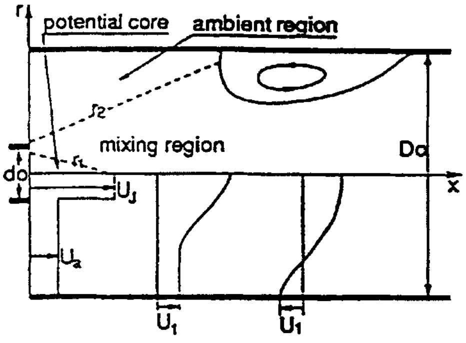

Figure 8. Flow configuration and notation

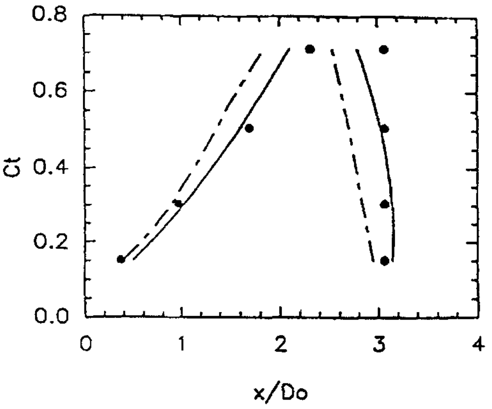

Figure 9. Separation and reattachment points (legend as in Figure 5)

3.5. *Confined swirling coaxial jets*

This is the case experimentally studied by Roback and Johnson.[20] Figure 11 shows the general features of the flow. At the inlet an inner jet and an annular jet are ejected into an enlarged duct. Besides an annular recirculation bubble due to sudden expansion of the duct, a centreline recirculation bubble is created by flow swirling. Figure 12 compares the calculation of the centreline velocity with the experiment. The negative velocity indicates the central recirculation. It is seen that both models predict the strength of central recirculation and the front stagnation point quite well, but the present model predicts the rear stagnation point much better than does the SKE model. Figure 13 shows the comparison of calculated and measured mean velocity profiles at $x = 5{\cdot}1$ cm. Both models give reasonably good profiles which are within experimental scatter, except for the peak values of the axial and radial velocities. Both models have been found to give nearly the same results in the downstream region, which can also be seen from Figure 12.

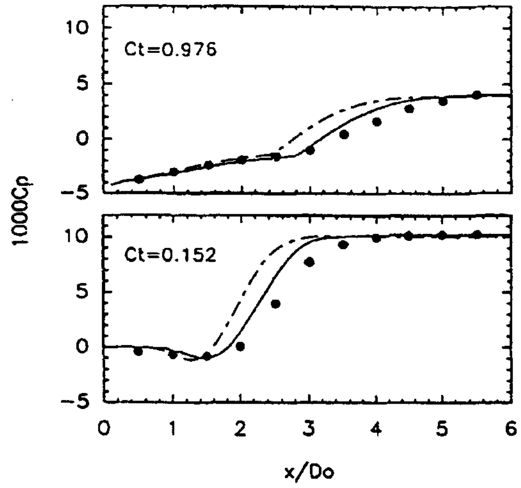

Figure 10. Pressure coefficient along duct wall (legend as in Figure 5)

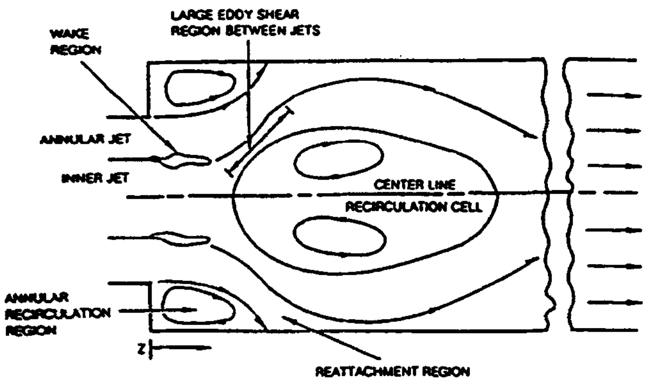

Figure 11. Flow configuration

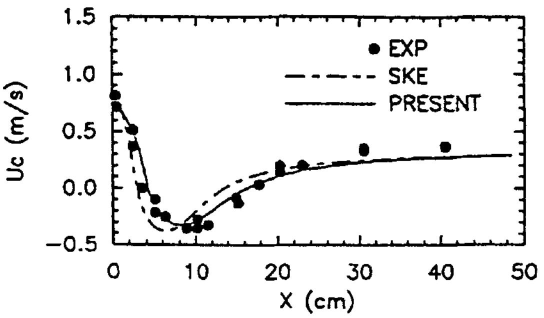

Figure 12. Centreline velocity

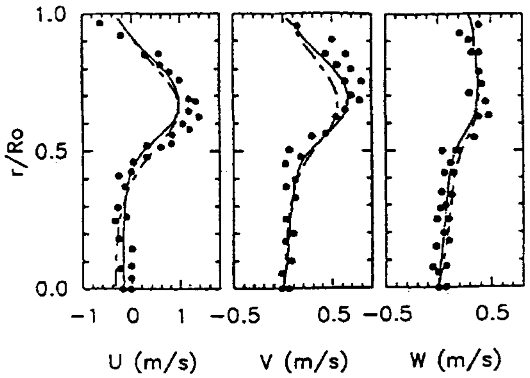

Figure 13. Mean velocity profiles at $x = 5{\cdot}1$ cm (legend as in Figure 12)

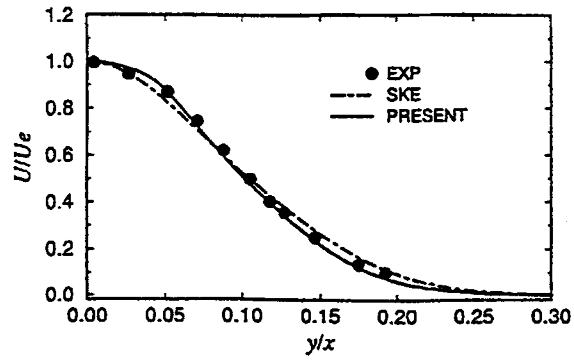

Figure 14. Self-similar mean velocity profiles for plane jet

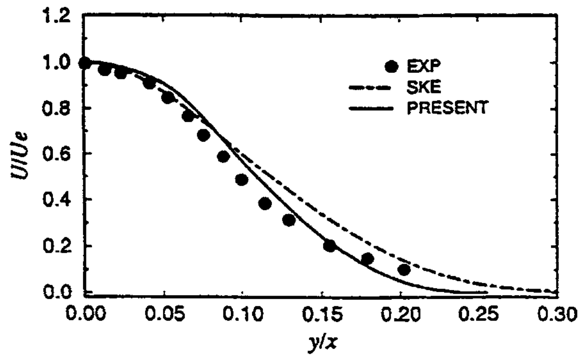

Figure 15. Self-similar mean velocity profiles for round jet

3.6. Turbulent free shear flows

Calculations were also performed for a mixing layer, a plane jet and a round jet. The results shown here are only for the jets owing to the space limitation. Figures 14 and 15 show the comparisons of the self-similar mean velocity profiles from the model predictions and the various measurements for the plane and round jets respectively. In Figure 14 the model predictions are compared with the measurements of Gutmark and Wygnanski[21] for the plane jet. The predictions given by both the present model and the SKE model agree well with the experimental data. For the round jet the comparisons are made between the model predictions and the measurements of Rodi[22] and are shown in Figure 15. The profile distribution of the mean velocity predicted by the present model agrees well with Rodi's data, while the SKE model predicts a faster spreading of the round jet into the surroundings and a wider distribution.

4. CONCLUSIONS

A realizable Reynolds stress equation model has been applied to calculate both complex wall-bounded flows and free shear flows. The calculations have been compared with available experimental data. The comparisons show that the present model provides significant improvement over the standard k–ε eddy viscosity model and that the present model is robust and economical as well. This indicates that the present model has good potential to be a practical tool in engineering applications.

ACKNOWLEDGEMENTS

The authors are grateful to Drs Z. Yang and W. W. Liou for their calculations of free shear flows and fruitful discussions. The work of J. L. Lumley was supported in part by Contract AFOSR 89-0226, jointly funded by the U.S. Air Force Office of Scientific Research (Control and Aerospace Programs) and the U.S. Office of Naval Research, and in part by Grant F49620-92-J-0038, funded by the U.S. Air Force Office of Scientific Research.

REFERENCES

1. S. B. Pope, 'A more general effective-viscosity hypothesis', *J. Fluid Mech.*, **72**, 331–340 (1975).
2. B. E. Launder, G. J. Reece and W. Rodi, 'Progress in the development of a Reynolds-stress turbulence closure', *J. Fluid Mech.*, **68**, 537–566 (1975).
3. D. B. Taulbee, 'An improved algebraic Reynolds stress model and corresponding nonlinear stress model', *Phys. Fluids A*, **4**, 2555–2561 (1992).
4. J. Zhu, 'FAST-2D: a computer program for numerical simulation of two- dimensional incompressible flows with complex boundaries', *Rep. 690*, Institute for Hydromechanics, University of Karlsruhe, 1991.
5. B. E. Launder and D. B. Spalding, 'The numerical computation of turbulent flows', *Comput. Methods Appl. Mech. Eng.*, **3**, 269– 289 (1974).
6. A. Yoshizawa, 'Statistical analysis of the derivation of the Reynolds stress from its eddy-viscosity representation', *Phys. Fluids*, **27**, 1377–1387 (1984).
7. R. Rubinstein and J. M. Barton, 'Nonlinear Reynolds stress models and the renormalization group', *Phys. Fluids A*, **2**, 1472–1476 (1990).
8. T.-H. Shih and J. L. Lumley, 'Remarks on turbulent constitutive relations', *Math. Comput. Model.*, **18**, 9–16 (1993).
9. R. S. Rivlin, 'Further remarks on the stress deformation relations for isotropic materials', *J. Arch. Rat. Mech. Anal.*, **4**, 681–702 (1955).
10. U. Schumann, 'Realizability of Reynolds stress turbulence model', *Phys. Fluids*, **20**, 721–725 (1977).
11. J. L. Lumley, 'Computational modelling of turbulent flows', *Adv. Appl. Mech.*, **18**, 124–176 (1978).
12. C. G. Speziale, 'On nonlinear *K–l* and *K–* ε, *J. Fluid Mech.*, **178**, 459–475 (1987).
13. T.-H. Shih, J. Zhu and J. L. Lumley, 'A realizable Reynolds stress algebraic equation model', *NASA TM 105993*, 1993.
14. D. M. Driver and H. L. Seegmiller, 'Features of a reattaching turbulent shear layer in divergent channel flow', *AIAA J.*, **23**, 163–171 (1985).
15. A. C. Trupp, R. S. Azad and S. Z. Kassab, 'Near-wall velocity distributions within a straight conical diffuser', *Exp. Fluids*, **4**, 319–331 (1986).
16. H. R. Fraser, 'The turbulent boundary layer in a conical diffuser', *J. Hydraul. Div.*, **HY3**, 1684.1–1684.17 (1958).
17. D. J. Monson, H. L. Seegmiller, P. K. McConnaughey and Y. S. Chen, 'Comparison of experiment with calculations using curvature-corrected zero and two equation turbulence models for a two-dimensional U-duct', *AIAA Paper 90-1484*, 1990.
18. J. Kim, S. J. Kline and J. P. Johnston, 'Investigation of separation and reattachment of a turbulent shear layer: flow over a backward-facing step', *Rep. MD-37*, Thermosciences Division, Department of Mechanical Engineering, Stanford University, 1978.
19. M. Barchilon and R. Curtet, 'Some details of the structure of an axisymmetric confined jet with backflow', *J. Basic Eng.*, **86**, 777–787 (1964).
20. R. Roback and B. V. Johnson, 'Mass and momentum turbulent transport experiments with confined swirling coaxial jets', *NASA CR 168252*, 1983.
21. E. Gutmark and I. Wygnanski, 'The planar turbulent jet', *J. Fluid Mech.*, **73**, 465–495 (1976).
22. W. Rodi, 'A new method of analyzing hot-wire signals in highly turbulent flow and its evaluation in round jets', *Disa Information, No. 17*, 1975.